A High Sensitivity System for Luminescence Measurement of Materials

Adrian A Finch[1], Yafang Wang[2], Peter D Townsend[3], Martin Ingle[4]

1 - School of Earth & Environmental Sciences, University of St Andrews, Fife KY16 9AL, UK.

2 - School of Science, China University of Geosciences, Beijing, 100083, China.

3 – Physics Building, University of Sussex, Brighton, BN1 9QH, UK.

4 - Photek Ltd., 26 Castleham Road, St Leonards on Sea, East Sussex TN38 9NS, UK.

Abstract

A unique combined and multi-disciplinary wavelength multiplexed spectrometer is described. It is furnished with high-sensitivity imaging plate detectors, the power to which can be gated to provide time-resolved data. The system is capable of collecting spectrally resolved luminescence data following x-ray excitation (radioluminescence, RL or X-ray excited optical luminescence, XEOL), electron irradiation (cathodoluminescence, CL) and visible light from LEDs (photoluminescence, PL). Time-resolved PL and CL data can be collected to provide lifetime estimates with half-lives from μs timeframes. There are temperature stages for the high and low temperature experiments providing temperature control from 20 to 673 K. Combining irradiation, thermal ramping and TR-PL allows spectrally-resolved thermoluminescence (TL) and optically stimulated luminescence (OSL). The design of two detectors with matched gratings gives optimum sensitivity for the system. Examples which show the advantages and multi-use of the spectrometer are listed. Potential future experiments involving lifetime analysis as a function of irradiation, dose and temperature plus pump-probe experiments are discussed.

Keywords:

Time-resolved spectroscopy; luminescence lifetime; thermoluminescence; cathodoluminescence; photoluminescence; x-ray excited optical luminescence; radioluminescence; luminescence instrumentation.

1. Introduction

Luminescence offers one of the most sensitive routes to understand the distortions and imperfections in insulating and semiconducting solids. The method benefits from the fact that emission spectra, temperature dependence and excited state lifetimes all differ, providing not only characterisation of different types of defect, but also evidence for distortions and clustering in the local environment of those structures. Additionally, luminescence can be excited by a wide range of energetic methods, from site selective photon excitation (PhotoLuminescence, PL, e.g. Friis *et al.* 2010), surface techniques with low energy electrons (CathodoLuminescence, CL, Townsend & Rowlands 2000) to bulk ionization methods using x-rays (either termed RadioLuminescence, RL or X-ray Excited Optical Luminescence, XEOL, Friis *et al.* 2011) or particle irradiation (IonoLuminescence, IL or Ion Beam Luminescence, IBL, e.g. Finch *et al.* 2004). Furthermore, one can selectively release charge from particular defect sites after irradiation as a function of temperature, thus providing the site specific information encoded in ThermoLuminescence (TL, Yang *et al.* 1998, Karali *et al.* 2000).

Modern optical detectors with high sensitivity and very low background noise levels mean that responses from impurity or defect sites can be detected well below parts per million (ppm) concentrations. Luminescence spectroscopies are therefore a particularly valuable family of techniques to characterize defect structures in materials, even at low concentrations. Because of the applicability of luminescence across disciplines, the relevant literature is spread across many sciences including condensed matter physics, radiation dosimetry, chemistry, geology, geography and archaeology (Wang & Townsend 2013). The only caveat is that, because of the diversity of applications and user expertise, not all the literature reports data that have been consistently or correctly processed and this may generate apparent differences that are artefacts of the experimental and data processing methods (Wang & Townsend 2013). With such a wide range of luminescence methods and extreme sensitivity to the target material, it is essential to make several types of measurement on a single sample to understand fully the information encoded in luminescence data. Consequently one requires a system which has programmable temperature control from e.g. 20 to 673 K, and that can apply all the excitation methods to excite PL, CL, RL and TL. Note also that previous systems often are only capable of ramping the temperature upwards, as for TL, but controlled cooling is equally valuable since it can separate contributions of TL from ramped CL/RL/PL and also reveal hysteresis and single event phase transitions (e.g. Yang & Townsend 2000). For some methods either steady state or modulated excitations are required, and from the latter we extract lifetime as well as emission spectral data.

The purpose of this article is to describe a unique luminescence system designed to address these technical and instrumental challenges. Its detectors have been developed in a partnership with the manufacturer (Photek Ltd) to provide state-of-the-art photon sensitivity combined with fast gating of the power to allow time-resolved spectroscopies. The instrument measures several types of luminescence spectroscopy,

including simultaneous multiple excitation, in both continuous wave and pulsed excitation modes as a function of temperature from 20-673 K. We illustrate the capabilities of the system with novel data from a selection of industrially relevant materials. We also outline potential future applications.

2. Design of the System

2.1 Introduction and History

In the early 1990s a system dedicated to the measurement of TL was designed with detection of wavelength multiplexed luminescence made possible by the use of photon imaging detectors (Luff & Townsend 1993) and housed at the University of Sussex, UK. The high f number optics (f/2.2) allowed the use of low heating rates for the TL so that there were minimal uncertainties between the heating stage temperature and the emission region at the surface of the samples (Ege *et al.* 2007). This was highly effective and, in addition to recording spectrally resolved TL over the wide temperature range, there were unexpected bonuses in peak temperature shifts related to pairing and clustering of impurities, or their association with different defect species (e.g. Kurt *et al.* 2001, Maghrabi *et al.* 2013). Since different polymorphs usually show different emission spectra, it was possible to detect phase transitions very rapidly in a dynamic heating or cooling run (Yang & Townsend 2001). Not only did this reveal hysteresis, but it showed a wide range of previously unsuspected crystalline transformations in materials as diverse as KTP, $SrTiO_3$, fullerenes and superconductors (see Wang *et al.* 2012 for a review). CL was used to probe the role of contaminants and surface relaxations (Rowlands *et al.* 1998). Dramatic changes in intensity were noted not only for phase transitions of the host materials, but also driven by phase transitions within inclusions of nanoparticles of impurities (or added dopants). This emphasises that there are very long range interactions from such inclusions that modify the entire sample. The Sussex system provided some of the most exciting and innovative discoveries in luminescence science of the last 25 years (e.g. Yang *et al.* 1998, Kurt *et al.* 2001, Wang *et al.* 2011, 2015).

On the retirement of Townsend, the system was brought to St Andrews, where new detector systems were installed, several improvements were made and new software was written. There is now a need to describe the modified system with its enhanced sensitivity and greater capabilities. Rather than describe the history of modifications to the system, we provide here a description in its current state, without differentiating between the original design and our subsequent modifications (Luff & Townsend 1993).

2.2 The Sample Chamber, Light Path and Stages

The system comprises a central chamber made out of aluminium (typically 3 cm thick) and brass (5 mm thick) to reduce x-ray leakage (Fig. 1). A USB webcam inside the chamber allows visualisation of the sample

on the stage. A two-stage vacuum system roughs down to 10^{-1} mbar (10 Pa) with an Edwards Rotary Pump and harder vacuum down to 10^{-6} mbar (0.1 mPa) using a Edwards 100/300 650 W Diffstak diffusion pump. The vacuum status is monitored using Edwards VSK1B vacuum switches and two Edwards APG100 active pirani gauge heads. The vacuum switches close when the vacuum is below a threshold (typically 10 mbar = 1 kPa) and the active vacuum heads provide output voltages between 0-6 V as an exponential function of vacuum. These voltages are monitored using a Velleman K8055 USB Experimental Interface board (http://www.velleman.eu/products/view/?country=be&lang=en&id=351346) and converted to an estimate of vacuum – the digital input channels are connected to the vacuum switches and other microswitches around the instrument.

The two-stage vacuum system is controlled by switching mains power on and off to the pumps (rotary and diffusion pumps) using a Measurement Computing USB-ERB08 Electromechanical Relay Interface (http://www.mccdaq.com/usb-data-acquisition/USB-ERB08.aspx). The ERB08 unit also operates the helium compressor, controls venting of the sample chamber during sample change and the safety interlock on the x-ray generator. The stage mounted is detected using microswitches and the program then automatically communicates with the appropriate stage. The system is interlocked for radiation safety and protection of the detectors.

To cover the entire spectrum from the UV to the IR, two detectors operate simultaneously, targeting the UV-Blue and visible-near IR regions, referred to as the 'blue' and 'red' detectors respectively. Each is housed in separate detector housings, either side of the chamber (Fig. 1). The light from the sample is focussed by two sets of two fused silica ('Spectrosil B') plano-convex lenses, a combination which provides 1:1 imaging of the sample on the entrance slits of the spectrometers. The lenses seal directly to the sample chamber, eliminating the need for additional windows in the sides of the chamber. In the case of the 'UV-blue' detector (see below), fused silica elements are necessary to enable UV transmission, but a further advantage of this material is its good resistance to radiation darkening. Since the lenses receive a considerable dose over time from scattered radiation in the chamber, fused silica is used for both lens combinations, even in the 'red' detector where UV is not measured. Lens combinations, rather than single lenses, are necessary to match the high f number of the spectrometers (f/2.2). Between the lenses and the entrance slits are lightproof boxes that accept standard (50 mm x 50 mm) filters. The entrance slits to the spectrometers can be swapped to modify the signal strength and spectral resolution, but the typical analysis takes place with 500 μm slits providing a typical wavelength precision of ~2 nm but widths of 125, 250 and 1000 μm are available. Manual shutters are placed in the light paths after the filter boxes.

The focal position of the spectrum is a function of wavelength, and hence the distances from the sample to each detector are different, optimised for the central wavelength region that each detector analyses (Luff & Townsend 1993). The light is diffracted by American Holographic Chemspec 100S gratings of the Rat-field

holographic type; one is used nominally for the range 200-450 nm (ref: 446.02/L) with a dispersion of 8 nm/mm and the other (ref: 446.14/L) from 400-800 nm with a dispersion of 12 nm/mm. The numerical aperture is f/2.2. The peak efficiency of each grating occurs at ~350 nm and ~730 nm, chosen near the centre of each spectral range, biased to enhance signals where the red photocathode sensitivity is falling steeply.

Second-order scattering of lower wavelengths into the first order spectrum will occur for the red grating detector, therefore a GG400 Schott Glass 400 nm long pass filter is permanently inserted into the light path of the red detector to remove the short wavelength signals (Fig. 1). The filter is not entirely opaque between 397-400 nm and for samples with a strong signal in this region, we observe a small second order response between 795-800 nm. Rather than attempt difficult corrections for this artefact, we accept that this remains in processed spectra of samples that are strong in the UV-Blue. The two detectors provide two separate sets of spectral data with a substantial overlap from which subsequent data processing creates a single composite UV-IR spectrum.

The chamber is furnished with two stages for cryogenic (20-300 K) and high-temperature (300-673 K) measurement. A third stage operating from -40 to +400^{o}C is also available for samples which have TL transitions around room temperature. The cryostage enters from below the chamber and the high temperature stage at the front; each has a blanking plate to isolate the chamber when the other stage is in use. The stage is a Cryophysics M22 cryostage, cooled by a CTI Cryogenics 8200 water-cooled Helium Compressor and heated with nichrome wire. Temperature is controlled by a Eurotherm 2404 controller connected to a Au-Fe thermocouple. The maximum ramp rate is 0.1 K s^{-1}. The cryostage is operated only when the sample has been in vacuum (<10^{-5} mbar = <1 mPa) for some hours, to avoid frosting of the sample. The higher temperature heating stages have a Nichrome strip 12 x 50 x 0.7 mm and a chromel/alumel thermocouple controlled by a Eurotherm 818P controller with switching accomplished by a Eurotherm thyristor unit model 462. The maximum ramp rate of the high temperature stage is 3 K s^{-1}.

2.3 The Detectors

The diffraction gratings deliver a strip of light onto the detector, such that the position of the photon arrival is a function of wavelength. The detectors are imaging plate detectors (ipds) manufactured to our specifications in a collaboration with Photek Ltd (www.photek.co.uk). Ipds were chosen to provide state-of-the-art sensitivity whilst also allowing sub-μs switching of the power to the detector plate for time-resolved luminescence experiments (see below). Cooled detectors were not favoured to avoid frosting of the detector – the difficulties associated with keeping the detector under vacuum or dry nitrogen were considered to overwhelm the benefits of lower dark current. IPDs use standard PM tube photocathode materials; however electron multiplication is provided by microchannel plates (MCP) rather than a dynode

chain. Charge clouds emerging from the channels are proximity focused onto a resistive anode. The current flow resulting from the original photon event is measured at four points on the resistive anode, enabling the position of the photon arrival and its arrival time to be reconstructed. Each ipd has a separate power unit and communicates to the master computer via USB. The 'blue' detector is a bialkali photocathode ipd; the 'red' detector is a S25 based photocathode – each detector type was chosen to maximise signal and minimise noise in the relevant spectral range. The dark current on each detector was typically 2.4 x 10^{-4} (blue) and 1.6 x 10^{-2} Hz nm^{-1} (red) but we observe a halo effect such that the dark current is lower in the centre and enhanced towards the edges. Following discussions between St Andrews and Photek, this foreshortening of the image was ameliorated against by an optional software patch. A fuller description of the imaging plate detectors is given in Supplementary Information 1. The position on the ipd is calibrated against wavelength using Hg, Kr emission lines and laser pointer sources and the output from the detectors are both raw images and reconstructed wavelength. Blackbody radiation in the infrared is seen as a background in all runs using the high-temperature stage above ~600 K and becomes progressively more intense as temperature rises to the maximum (673 K).

The system and detectors used here exploit the high sensitivity and dynamic range of photocathode detectors. However, they have a weakness in that their performance falls at long wavelengths. By contrast one can use CCD signal collection which functions into the near infrared region. Our system has sufficient access ports that in principle it is simple to add a fibre optic link to a longer wavelength CCD spectrometer for those materials which require such data. We have used CCD systems successfully during the recording of ion beam excited luminescence (Townsend 2012) and synchrotron-based XEOL (Taylor *et al.* 2013).

2.4 Sample Excitation

Three forms of excitation are available; 1) a Philips MCN-101 ceramic x-ray tube placed at the rear of the chamber, 2) an electron gun (taken from a Jeol electron microscope) on the top and 3) LEDs inserted inside the chamber and controlled by power sources externally. The x-ray and electron gun sources were controlled manually by units in the electronic rack. The x-ray controller is not operated above 30 kV and 15 mA to avoid x-ray leakage; typical operating conditions are 20 kV and 4 mA, providing dose rates of 1.8 Gy min^{-1}. The electron gun operates between 10 and 25 kV acceleration voltage with a typical beam current of 200 nA and a spot size typically with a diameter of 3 mm, providing an incident power density of ~1 kW m^{-2}. The beam is focussed using the electron optics inherited from the electron microscope source, controlled by external power supplies. Beam position (x-y) is tweaked using external magnetic fields generated by solenoids controlled by power supplies; beam pulsing is achieved by sudden increases in the current applied to these, flipping the beam off the sample. The LEDs are sourced either from RadioSpares (uk.rs-online.com) or Roithner LaserTechnik GmbH (www.roithner-laser.com) and controlled via an amplifier built

in-house and operated by a logic signal to be either on or off. Emission wavelengths down to 300 nm have been used although deeper UV LEDs are now available. Continuous wave photoluminescence (PL) is difficult since the excitation would saturate the sensitive detector plates. It can be achieved with the use of notch or long pass filters, or by exciting in the UV and only using data from the Visible-NIR detector. Time-resolved PL is achieved without the use of filters by <ms switching of the LEDs coupled to rapid switching of the detectors.

2.5 System Software

Software was written in-house using LabVIEW 2016 (www.ni.com/labview/) to operate from a Graphical User Interface (GUI). All automated components of the system are controlled by LabVIEW drivers but some were provided in other languages (e.g. visual basic or C) and adapted using LabVIEW wrappers. LabVIEW drivers for the stages are downloaded from National Instruments and adapted for the present system. The Eurotherm 818 controller (high temperature stage) uses a version of an older 808 driver by enabling extra commands compatible with the 818. The Eurotherm 2404 controller (low temperature heating stage) is successfully operated via a generic 2400 series driver. Both controllers work via RS232 protocol, operated via USB using a 4-way USB-RS232 converter.

The detectors come with Photek software (Image32) which can be operated directly or controlled from LabVIEW using wrappers provided by Photek. Photon arrivals are accumulated over preset integration periods, assigning a position on the imaging plate and a time stamp to every photon arrival. The output is a 16-bit monochrome image covering the entire detector area. Photon arrival events outside the rectangular area illuminated by the grating are rejected. Direct image transfer from the Photek software to LabVIEW results in the loss of the most significant bit in the data, and hence the program writes the image data to the hard drive from Image32 and reads it back into LabVIEW as a 16-bit image using routines in the LabVIEW Image Module. For continuous wave (CW) measurements, the time stamps are ignored and the two-dimensional image from each detector is converted to a 1D spectrum by summing individual pixel values onto the wavelength axis.

For time resolved (TR) analysis, excitation is pulsed and photon arrivals in the 'off' cycle are analysed as a function of wavelength and arrival time. Since the power to the ipd is switched off during this cycle, time-resolved photoluminescence (TR-PL) is possible without any filters since the intense light from the LED arrays do not encounter the detector whilst the voltage is on, thereby avoiding damage to the detector. TR analysis uses LED (time-resolved PL, TR-PL) or electron beam excitation (TR-CL). The electron beam is pulsed by flicking the beam off the sample using an electromagnet on the column; LEDs are controlled by pulsing the power to them. We observe ~1 μs phosphorescence from standard LEDs after the power is stopped. Although nano-LEDs with rapid switching are available, we have found it more convenient to use

cheaper standard LEDs and insert a software delay (typically 3 μs) between the end of the 'on' excitation signal and powering up the detectors. Blank measurements with the delay show no sign of the primary excitation in TR-PL. Photon arrival times during data acquisition are binned over multiple iterations producing a 16-bit rectangular image with wavelength on one axis and numbers of photons per time bin on the other. Time bin widths are software controlled but are typically 250 ns, 200 bins and integration times of 5 minutes provide data that we have processed successfully (see below) to provide estimates of lifetime in the μs to s range.

Longer (seconds to hour length) lifetimes are measured using a 'phosphorescence' routine in LabVIEW whereby repeated CW spectra are collected and then amalgamated to create a 2D image. The outputs from this type of analysis emulate those of TR analysis so that the same software routines are applied.

2.6 Offline Data Processing and Manipulation

We store data as raw files and system corrections are performed off line. This allows alternative system corrections and data manipulation to be performed retrospectively without the need to reconstruct raw images. We have preferred this approach particularly since offline processing software is regularly improved. The data from the individual detectors are corrected first by subtracting the dark current (as a function of wavelength and exposure time), then dividing by the system responses of the two ipds (Fig. 2, provided by Photek). The gratings are blazed for optimum efficiency in the centre of the range and fall to about 50% grating efficiency at half and double the blaze angle. We model the grating efficiencies as a parabolic function of log of wavelength centred on the blaze wavelength. Because we focus on the central portions of each grating, the efficiency across the majority of the data range is >90%, and might reasonably be considered essentially constant. However there is a significant dip below 250 nm, and an inconsistency between the efficiencies of the two gratings in the overlap region. We therefore correct the data using our grating efficiency model. Although this is a first order correction, it amplifies the deeper UV data and improves the fitting of the two spectra (R^2 are increased, see below). The effects of the transmission of the quartz lenses (and the 400 nm long pass filter in the red detector) are also accommodated. The two spectra are matched in the overlapping spectral region, typically 420-480 nm, avoiding the edge regions of both spectrometers where the dark current is high and image foreshortening is observed. Because of the steric effects of the sample and different focus distances to the two imaging plates, the amount of light arriving at the two detectors is never perfectly matched in intensity. We scale the two images with respect to each other to accommodate, with the overlap region comprising a linear combination of the two images. We calculate a fit index (R^2) to express how the two images match with linear scaling. Where significant signal is present, R^2 values >95% are observed. Analysis of single emission band profiles in energy space give Gaussian fits, suggesting that our system corrections provide accurate and undistorted final profiles. At

temperatures above 600 K (~320°C), significant blackbody radiation is observed in the spectra at 800 nm which increases and creeps to shorter wavelengths with increasing T. The blackbody radiation from the stage is often many orders of magnitude greater that the luminescence signals from the samples, hence the data for the high temperature stage are deleted where significant blackbody radiation occurs in a sample blank.

The final outputs are transferred automatically to ORIGIN for plotting and standard 3D and contour plots (used in the present study) are generated automatically. These are typically contoured with 'hot' colours to express higher counts and 'cold' colours as lower ones (e.g. Figures 3, 4). However in recognition of the many in the science community who are colour blind (including one of us), the software also generates monochrome contour-based outputs which we present in Supplementary Information 2. Examples of the raw and processed data formats are attached to the present article as Supplementary Information 3.

3 Examples of Luminescence Data

We present data below from a cross-section of materials designed to explore and test the accuracy and capabilities of the system. We have used both well-characterised samples, whose data can be related to the open literature, and a selection of more challenging materials which provide novel observations and provide insights into the future capabilities of the system and the types of scientific questions that this system might address. Data are collected using both the high temperature and cryogenic stages.

3.1 TL and Dosimeter Materials

GR200 is one of the most commonly used dosimeters for the personal radiation dosimetry. High Temperature TL data for GR200 were collected in the temperature range from 20 to 400 °C after 2 Gy x-irradiation (Figure 3). In order to minimize temperature gradients across the sample, a heating rate if 0.1 K s^{-1} is usually employed. In this example, the TL of the sample occurs at 188°C with a wavelength maximum at 381 nm. As can be seen from Figure 3, the TL of this material is particularly effective dosimeter material using conventional TL (spectrally unresolved) since its peak emission in the blue/near UV is close to the optimum quantum efficiency of a photomultiplier tube (PMT, typically ~400 nm). However many commercial TL systems use PMTs with glass windows which are opaque in the UV and also contain infrared filters to protect the photocathode, but which also partially attenuate the target signal. As a result, despite the extra dimension of spectral resolution, our system performs favourably in terms of its UV sensitivity compared to commercial systems.

Figure 4 shows a 3D plot of TL from a $MgSiO_4$:Tb dosimeter material (Tawara *et al.* 2011). The Tb emission lines are dominant and extend across the UV and visible. The irradiation was 100 Gy and the heating rate was 0.25 K s^{-1} over the temperature range from 25 to 400 °C. We observe emissions at 379, 417, 440, 483,

550, 583 and 621 nm (consistent with the published spectrum of McAllister 1966) and maxima at 35, 133 and 293°C. This material is a particularly useful test since the spectrum is the product of the two separate detectors and are 'stitched' together to provide a single spectrum. The wavelengths of the example demonstrate that not only can the system readily resolve the Tb emission lines, but also the data obtained from the two separate detector units are successively resolved into a single spectrum. The wavelength peaks are consistently within a few nm of the expected values, the reported accuracy of the spectrum.

Figures 3 and 4 show that TL can be readily observed, not only providing the glow peak temperature, but also spectral resolution (cf. Wang *et al.* 2017). We readily observe TL in less sensitive dosimeter materials, including alumina (Chithambo *et al.* 2015), quartz, feldspar and sodalite (Finch *et al.* 2016). We improve signal-to-noise in the least sensitive materials by increasing the initial dose (longer x-irradiation times) and/or the temperature ramp rate. Faster ramp rates produce more photons per second, and therefore a better signal to noise for weak signals, although a discrepancy between the temperatures of the sample and the thermocouple may be evident at the highest ramp rates.

Figure 5 shows the Low Temperature TL of pink sodalite ($Na_8Al_6Si_6O_{24}Cl_2$). The data show four glow peaks at 66, 105, 190 and 232 K. However the 66 and 232 K TL peaks occur at 690 nm whereas the 105 and 190 K peaks predominantly lie in the UV and blue (309 and 411 nm). The spectroscopic resolution of the system allows the shift in the wavelength of the TL to be observed, something that is absent from conventional spectrally-unresolved TL. This material is discussed further below.

3.2 XEOL and Phosphors

X-irradiation delivers photons with energies equivalent to the binding energies of core electrons. X-irradiation liberates core electrons and the subsequent luminescence (XEOL or RL) derives from energy cascades as electrons fall into the empty core electron states. To explore the efficacy of the system at measuring XEOL, we present data for a natural sodalite. XEOL often provides relatively bright signals compared to TL. Each pixel on the detector plate has a maximum bin depth of 2^{16} counts, and bright samples saturate the bins. Furthermore, very fast accumulation is associated with non-linearity in the relationship between counts and brightness and the very brightest signals trip the internal protection software for the detector, switching the power to the detectors off. For these reasons, brighter materials are accommodated by reducing integration times (making sure individual pixels in the image do not saturate) and/or light attenuation including a) smaller slits before the gratings and/or b) the use of pinholes and neutral density filters. Normally we repeat experiments which have used the highest bit of any pixel on the image.

For dimmer materials, we integrate for longer, and increase the slit width before the gratings, accepting that this results in a loss of wavelength resolution. The system is normally operated with 500 μm slits but these can be opened to 1000 μm, broadly increasing signal 4-times. Dimmer materials such as diamond, quartz and feldspar have been successfully measured on the system, but here we present novel data for the framework silicate sodalite (Finch *et al.* 2016). XEOL data can be obtained as a function of temperature and incident power (e.g. Wang *et al.* 2015). The XEOL as a function of temperature of a pink sodalite (AF-07-35) is presented in Figure 6. This shows a strong broad band in UV-blue with a less intense peak in the red-NIR. A feature of the data are notable peaks in the red-NIR band at 66 and 105 K and localised broadening of the UV-blue band at 105 and 190 K, observed as a stripe across the data at that temperature. Comparison of the XEOL of the sample (Figure 6) with the TL (Figure 4) show that these features correspond to TL peaks in the sodalite. The XEOL data are collected at a relatively fast ramp rate (0.1 K s^{-1}) to allow the spectrum to be collected in a convenient timeframe. However, with continuously increasing temperature, the data produced are actually a composite of the XEOL and TL behaviour, which we call 'XEOLTL'. Normally we infer the isolated XEOL behind the TL without further experimentation, but the TL contribution to the data can be diminished by a) slowing the temperature ramp rate b) inserting pauses at each temperature before the light is measured or c) measuring the XEOL during the cooling cycle.

The sodalite data are of particular interest, since the 66 and 232 K TL occur in the red-NIR region (Figure 4), whereas XEOL at the same temperature is dominated by the UV-Blue emission (Figure 6). We interpret this to indicate that there is coupling of the trap (in both energy and spatial senses) and the recombination site. Observations such as this provide not only direct evidence for the coupling of electron traps and recombination centres, but also potentially insights into the physical nature of traps in dosimeter materials.

3.3 Structural Phase Changes

Luminescence data have long been used to study imperfections and to characterize lattice distortions since the signals are sensitive to changes of structure (particularly point symmetry) and composition. Previous work has included intentionally added probe ions, such as lanthanides, to sense distortions in local crystal fields caused by modified structural environments. An underexploited extension of this approach is to use luminescence to monitor crystalline phase changes. Figure 7 shows XEOL of a $SrTiO_3$ crystal from 20 to 300 K with the heating rate of 0.1 K s^{-1} (Wang *et al.* 2015). Very strong changes in wavelength and intensity of the luminescence accompany the region between 50 and 80 K, the temperature window in which $SrTiO_3$ undergoes phase transitions (Hasegawa *et al.* 2000). The temperature profile of the NIR emission shows a maximum at 78 K and a point of inflexion in intensity at 180 K (Figure 7). We also show the first derivative of those data with respect to Temperature (dI/dT). Phase transition temperatures are most closely

approximated by maxima in the first derivatives of intensity – here the transition appears as a two stage process with a maximum at 73 K, within a few K of the published inversion temperature (70 K).

Phase transitions are often associated with strong TL, and we have designed the system so that contrasts in luminescence lifetime can also be explored. All of these methods are sensitive probes of structural state in which phase transitions are particularly evident.

3.4 PL and Luminescence Lifetime Measurement

The instrument measures light emitted from X- or electron-irradiation in continuous mode, i.e. the excitation and detectors are on simultaneously. Photoluminescence (PL) can be measured in continuous wave mode by closing off one of the detectors (e.g. the UV-Blue) and exciting in that range, whilst measuring the response in the Visible-NIR spectrometer, or by the use of notch filters. However, thanks to fast switching of the power to the detectors and by pulsing the laser diodes, the light emitted from the sample is measured while the laser diode is in the 'off' cycle. No filters are necessary and the spectra measured can include the wavelength of the excitation. The acquisition rates of the detectors are such that only luminescence with lifetimes in μs or longer can be measured. The data can be acquired as a single spectrum, providing a single snapshot of the luminescence spectrum a few μs after the commencement of the off cycle. Such data are useful where light intensities are poor and merely an impression of the longer (>1 μs) lifetime components of a PL spectrum is sufficient. However it is usually more informative to collect multiple time slices from the spectra, providing a 3D graph comprising wavelength (x), time (y) and light intensity (z) which can be expressed in either contour or 3D graphical formats (Figure 8). Intensities are system corrected so that different parts of the spectrum can be directly compared. The instrument set-up allows different lifetimes to be measured simultaneously in different parts of the spectrum. For example, the time-resolved luminescence at 145 K of a $CaSO_4$:Tm,Li phosphor has been studied using PL excitation with 460 nm LEDs (Figure 8). The decay of Tm^{3+} luminescence is clear, resulting from the Tm^{3+}: $^1G_4 \rightarrow {}^3H_6$, $^1G_4 \rightarrow {}^3F_4$ and $^3F_3 \rightarrow {}^3H_6$ transitions whose wavelengths are at 477, 655 and 698 nm respectively (Giri *et al.* 2008). Visual analysis of the graph shows the presence of a broad band around 620 nm and the Tm^{3+}: $^3F_3 \rightarrow {}^3H_6$ doublet at 698 nm that are constant through the timeframe of the experiment. Time slices can be extracted from the data and modelled to provide estimates of decay lifetimes (Figure 8d). The half-life of the blue emission is consistent with a single exponential decay lifetime (τ) of 582±3 μs. Lifetimes in the ms range are commonly reported for f-f transitions within Tb^{3+} (e.g. Kroon *et al.* 2014), although this can be reduced by coupling the local environment, particularly inter-lanthanide energy transfer (e.g. Padlyak & Drzewiecki 2013). The orange emission comprises two components, one of which is long (>2.5 ms) and the other is similar to the lifetime of the blue emission (Figure 8d). The key point is that the system can resolve

in a single session the lifetimes of all the emissions in the spectra range and provide independent lifetime estimates.

4 Future Directions

The new system is designed to allow novel luminescence experiments to be performed. Earlier data have shown that the signals generated by PL, CL or RL independently not only offer different spectra (as expected) but, when two excitation sources are combined, the resultant signal is not the sum of the two separate processes (Townsend PD, unpubl data, 2018). The opportunities for these more subtle probes have now been implemented in the layout of the experimental sample chamber, including pump-probe experiments where one excitation is continuous and another is pulsed. Such experiments explore, for example, the luminescence of excited states. The software currently collects the data from one cycle (either 'off' or 'on') and protects the detector by switching the power off for the other. A pump-prime experiment can be achieved by two separate configurations, each measuring the 'off' and 'on' cycles separately, so long as the excitation is invisible to the detector (by stimulating in e.g. the IR or by exciting in the UV and switching the UV-Blue detector off). In such an experiment, there is no reason why the detector could not remain on for both cycles, but binning the data separately such that the responses of both off and on cycles are provided as independent images. This would allow data from both cycles to be collected simultaneously in a single experimental run. Although the existing software is currently not configured to allow this, Photek have indicated that such an upgrade is relatively easy.

The time-resolved capabilities of the system open a wide range of photoluminescence spectroscopies. Triplet states with wavelengths similar to those of the excitation can be measured (normally long pass filters remove data close to the excitation wavelength) and we can compare and contrast in real time direct excitation (where the luminescence is measured at energies below excitation) with stimulation and up-conversion (which are slow, i.e. >μs lifetimes and where the spectrum is analysed at energies above the energy of the incident light). Spectrally resolved Optically Stimulated Luminescence – a spectrally resolved variant of a widely used method in retrospective dosimetry – is feasible.

The ability to quantify spectra in the time domain allows luminescence lifetime to become a parameter in the characterisation of our materials. Our current methods for analysing time-resolved data are manual and automated analysis is necessary to analyse larger volumes of data. Fitting of spectra as surfaces is being developed, so that fluorescence emissions which overlap in both lifetime and wavelength can be resolved. Such data will be important in separating the competing luminescence from e.g. the same ion on non-equivalent crystallographic sites. In addition, where the wavelength of the emission is consistent with one emission band, but analysis of lifetime indicates both fast and slow components, this may indicate coupling of the luminescence centre with a non-radiative defect (i.e. Förster resonance). Such data provide

insights into e.g. defect clustering and the distribution of ions over non-equivalent sites. Experiments which include analysis of wavelength, lifetime, temperature and light intensity create substantial 4D datasets, which require data reduction to be readily understandable. We are developing software to allow lifetimes to be extracted automatically from such data and then compared from one run to the next as a function of temperature, exploring the dependence of lifetime and wavelength on temperature. We have no doubt that the flexibility of the system will allow other experiment types to be achieved.

5. Acknowledgements

We would like to thank the support of the Fundamental Research Funds for the Central Universities of China, the National Science Foundation of China (No.11205134) and Beijing Higher Education Young Elite Teacher Project (YETP0640). The refurbishment of the RLTLCL system at St Andrews was funded by NERC grant NE/H002715/1.

6. References

Chithambo ML, Nyirenda AN, Finch AA & Rawat NS (2015) Time-resolved optically stimulated luminescence and spectral emission features of α-Al_2O_3:C. *Physica B* **473**, 62-71.

Ege A, Wang Y & Townsend PD (2007) Systematic errors in thermoluminescence, *Nucl Insts and Methods A* **576**, 411-416.

Finch AA, Friis H & Maghrabi M (2016) Defects in Sodalite-Group Minerals Determined from X-ray Induced Luminescence. *Physics and Chemistry of Minerals*, **43**, 481-491.

Finch AA, Hole D, Townsend PD, Garcia-Guinea J & Hanchar JM (2004) Ionoluminescence of Zircon: Rare Earth Emissions and Radiation Damage. *Journal of Physics D: Applied Physics* **37**, 2795-2803.

Friis H, Finch AA & Williams CT (2011) Multiple luminescent spectroscopic methods applied to the two related minerals, leucophanite and meliphanite. *Physics and Chemistry of Minerals* **38**, 45-57.

Friis H, Finch AA, Williams CT & Hanchar JM (2010) Photoluminescence of zircon ($ZrSiO_4$) doped with REE^{3+} (REE = Pr, Sm, Eu, Gd, Dy, Ho, Er). *Physics and Chemistry of Minerals* **37**, 333-342.

Hasegawa T, Shirai M & Tanaka K (2000) Localising nature of photo-excited states in $SrTiO_3$. *Journal of Luminescence* **87-89**, 1217-1219.

Karali T, Can N, Townsend PD, Rowlands AP & Hanchar J (2000) Radio- and Thermo-luminescence of rare earth element and phosphorus-doped zircon. *American Mineralogist* **85**, 668-681.

Kroon RE, Swart HC, Ntwaeaborwa OM & Seed Ahmed HAA (2014) Ce decay curves in Ce, Tb co-doped LaF_3 and the energy transfer mechanism. *Physica B: Condensed Matter*, **439**, 83-87.

Kurt K, Ramachandran V, Maghrabi M, Townsend PD & Yang B (2001) Influence of phase transitions of ice on near surface Cathodoluminescence. *Journal of Physics: Condensed Matter* **14**, 4319-4328.

Luff BJ & Townsend PD (1993) High sensitivity thermoluminescence spectrometer. *Measurement Science and Technology* **4**, 65-71.

Maghrabi M, Zayed O & Finch AA (2013) radio- and Thermo-luminescence of single-doped and codoped lithium sodium sulfate. *Radiation Effects and Defects in Solids*, http://dx.doi.org/10.1080/10420150.2013.807514.

McAllister WA (1966) Luminescence in Mg2SiO4:Tb,Li Phosphors. *Journal of the Electrochemical Society* **113**, 226-229.

Padlyak B & Drzewiecki A (2013) Spectroscopy of the CaB_4O_7 and $LiCaBO_3$ glasses, doped with terbium and dysprosium. *Journal of Non-Crystalline Solids*, **367**, 58-69.

Rowlands AP, Peto A, Townsend PD, Chandler PJ, Harmer S, Hole DE, Olivares J & Randall DP (1998) Effects of surface defects on luminescence of Nd:YAG. In: *Luminescence Materials VI*, Ronda CR & Welker T (eds) Electrochemical Society, Pennington, USA, **97-29**, 165-176.

Tarawa H, Masukawa M, Nagamatsu A, Kitajo K, Kumagai H & Yasuda N (2011) Characteristics of Mg_2SiO_4 :Tb (TLD-MLS-S) relevant for space radiation dosimetry. *Radiation measurements* **46**, 709-716

Taylor RP, Finch AA, Mosselmans JFW & Quinn PD (2013) The Development of a XEOL and TR-XEOL detection system for the I18 microfocus beamline, Diamond light source. *Journal of Luminescence* **134** 49-58.

Townsend PD (2012) Variations on the use of ion beam luminescence. *Nucl Inst Methods B* **286**, 35-39.

Townsend PD & Rowlands AP (2000) Information encoded in cathodoluminescence spectra. In: *Cathodoluminescence in Geosciences*, Pagel M, Barbin V, Blanc P & Ohnenstetter D (eds) pp 41-57, Springer, Berlin.

Wang Y, Yang B, Can N & Townsend PD (2011) Indications of bulk property changes from surface ion implantation. *Philosophical Magazine* **91:2**, 259-271

Wang Y, Zhao Y, White D, Finch AA, Townsend PD (2017) Factors controlling the thermoluminescence spectra of rare earth doped calcium fluoride. *Journal of Luminescence*, **184**, 55-63.

Wang Y, Zhao Y, Zhang Z, Zhao C, Wu X, Finch AA & Townsend PD (2015) Energy Dependence of radioluminescence spectra from strontium titanate. *Journal of Luminescence* **166**, 17-21

Wang Y & Townsend PD (2013) Potential problems in collection and data processing of luminescence signals. *Journal of Luminescence* **142**, 202-211.

Yang B & Townsend PD (2001) Optical Detection of Phase Transitions in potassium niobate. *Journal of Modern Optics* **48**, 319-331.

Yang B, Townsend PD & Rowlands AP (1998) Low temperature thermoluminescence of rare earth doped lanthanum fluoride. Physical review B 57, 178-188.

6. Figures

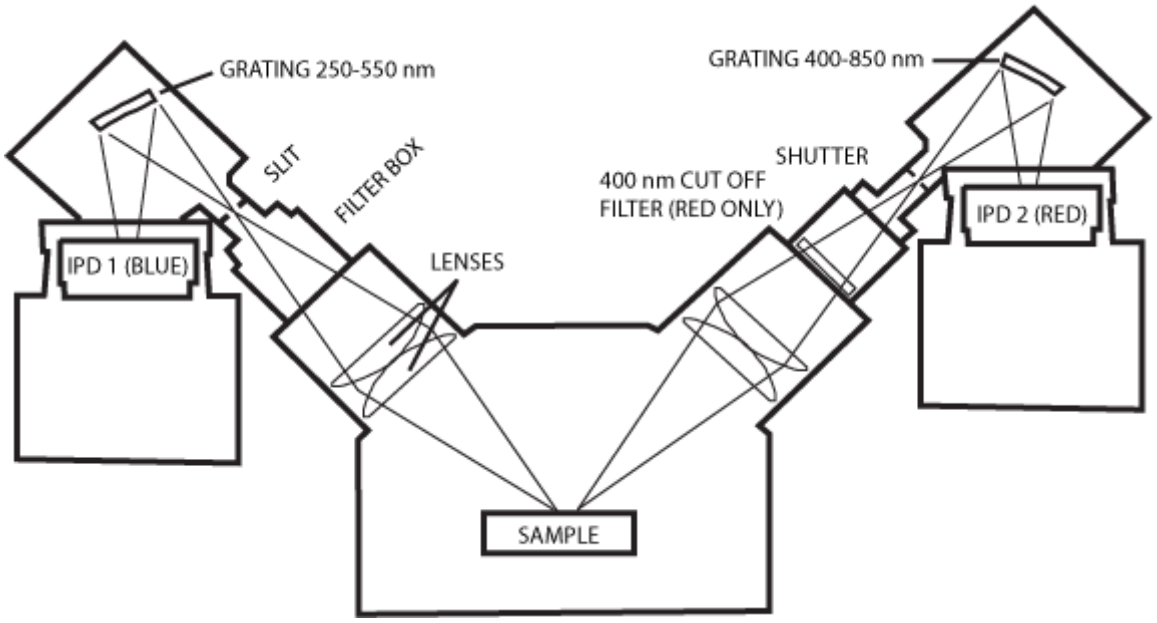

Figure 1: Schematic of the Luminescence System Chamber and Detector Arrangement. Detection is via two separate detector housings, which cover the region 250-550 nm ('Blue Detector') and 400-850 nm ('Red Detector'). The light paths to each detector are slightly different to make sure that each is focussed onto the ipd. Excitation of the sample comes from the top. The lenses, filter boxes, shutters and slits are common to both detectors but only labelled on one side for clarity. The 400 nm long pass filter is present only on the 'red' detector.

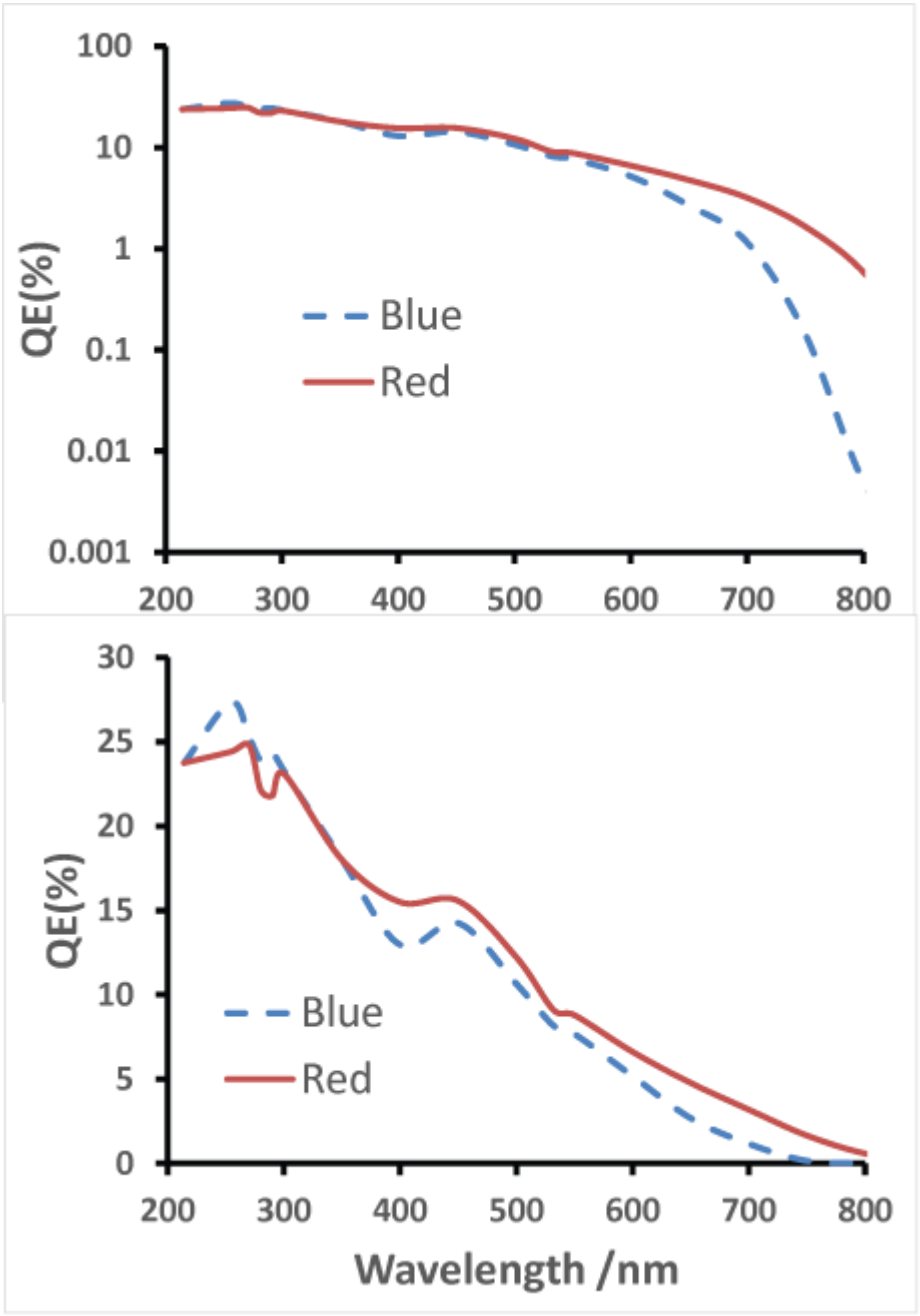

Figure 2: Relative Quantum Efficiencies (QE) of the ipd Detectors. The UV-blue detector is shown as a dashed blue line and the 'red' detector as a solid red line. Data are shown on both log and linear y-axis scales so that the relative efficiencies in the visible and the IR can both be understood. The bialkali ipd used on the UV-Blue detector has better performance in the UV, whereas the S25 detector has better performance in the visible and infrared.

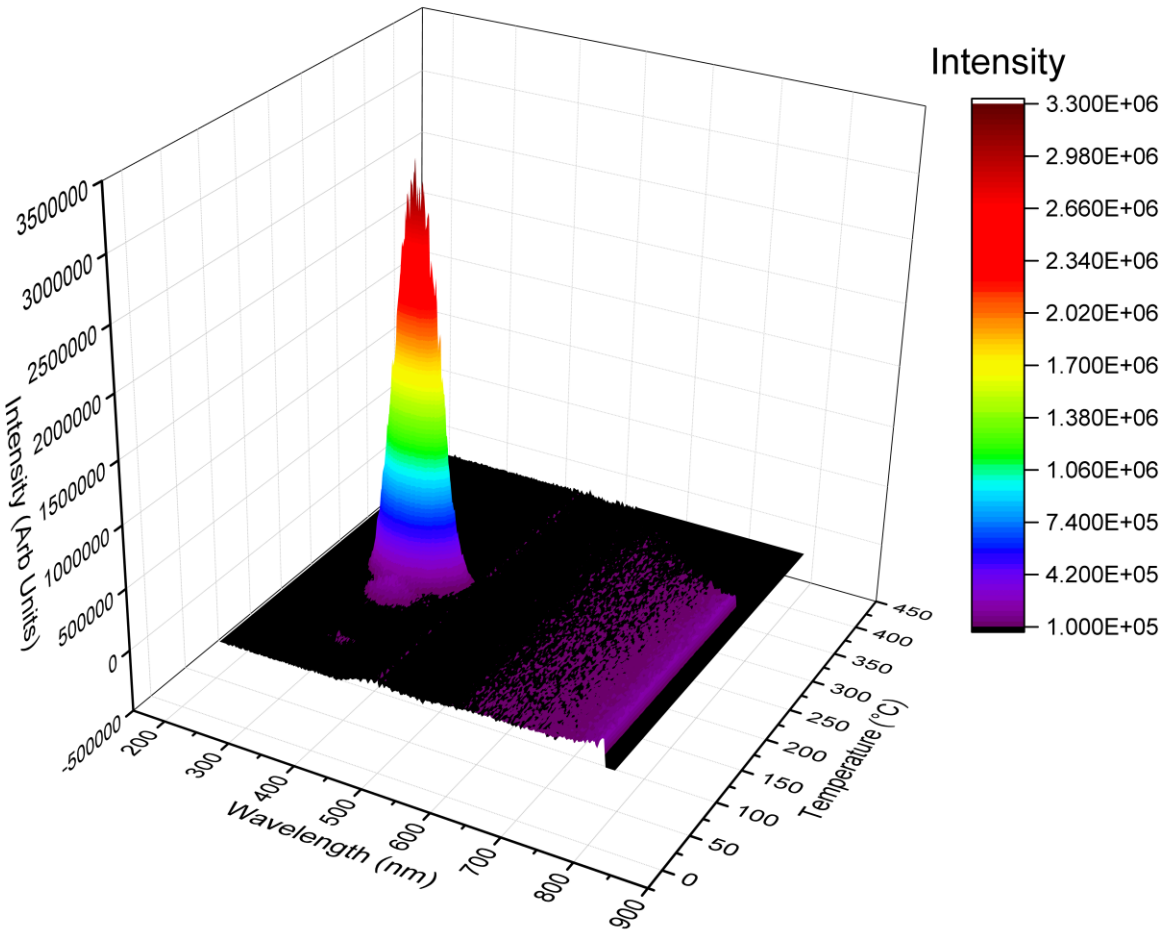

Figure 3: High Temperature TL of GR200 dosimeter material expressed as a 3D graph. Data are system corrected and the region of the spectrum where significant blackbody radiation is observed (above 320°C at 800 nm and moving diagonally across the graph) has been deleted. The strong TL emission centred at 381 nm and 188°C is clearly visible. Such data are an improvement over conventional TL measurements which have no spectral component.

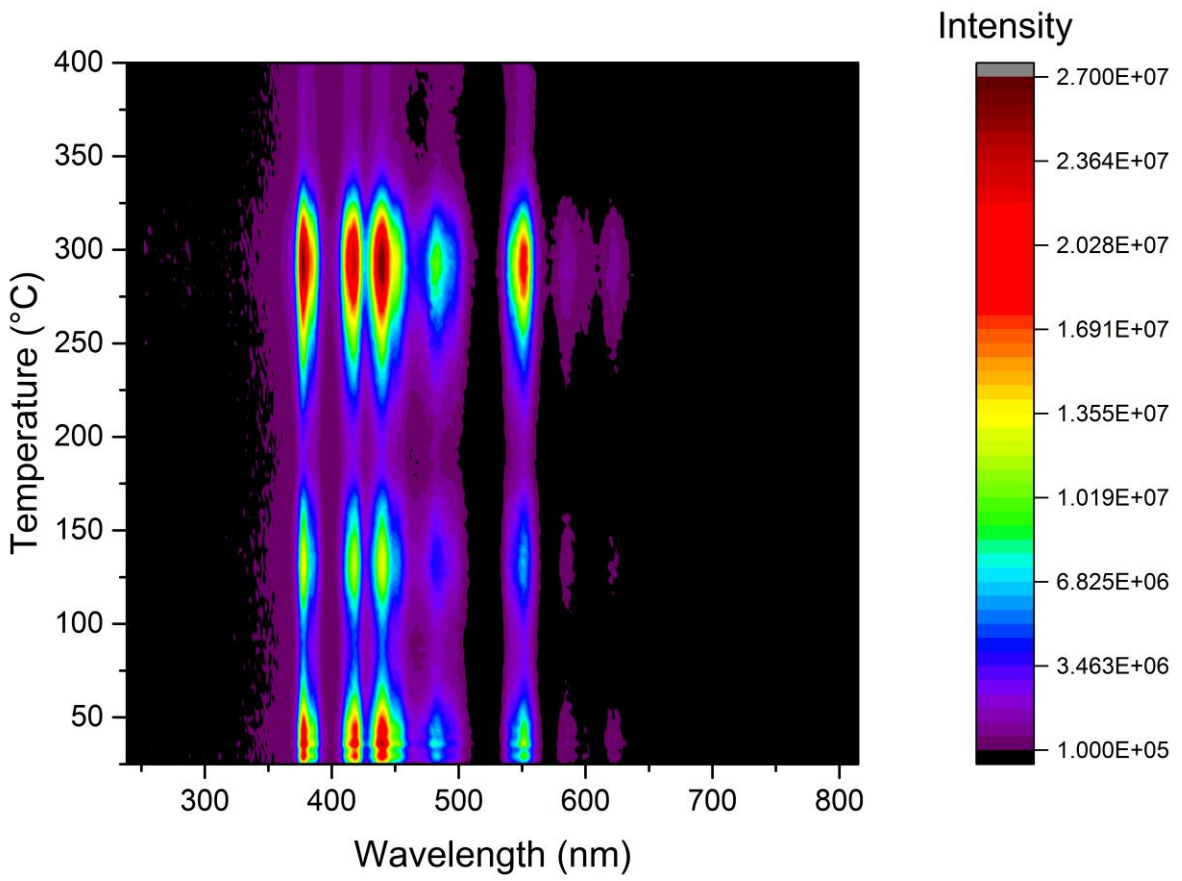

Figure 4: High Temperature **TL of Mg_2SiO_4:Tb expressed as a contour plot.** Tb emissions at 376, 417, 438, 483, 550, 586 and 621 nm are observed and TL glow peaks occur at 35, 133 and 293°C.

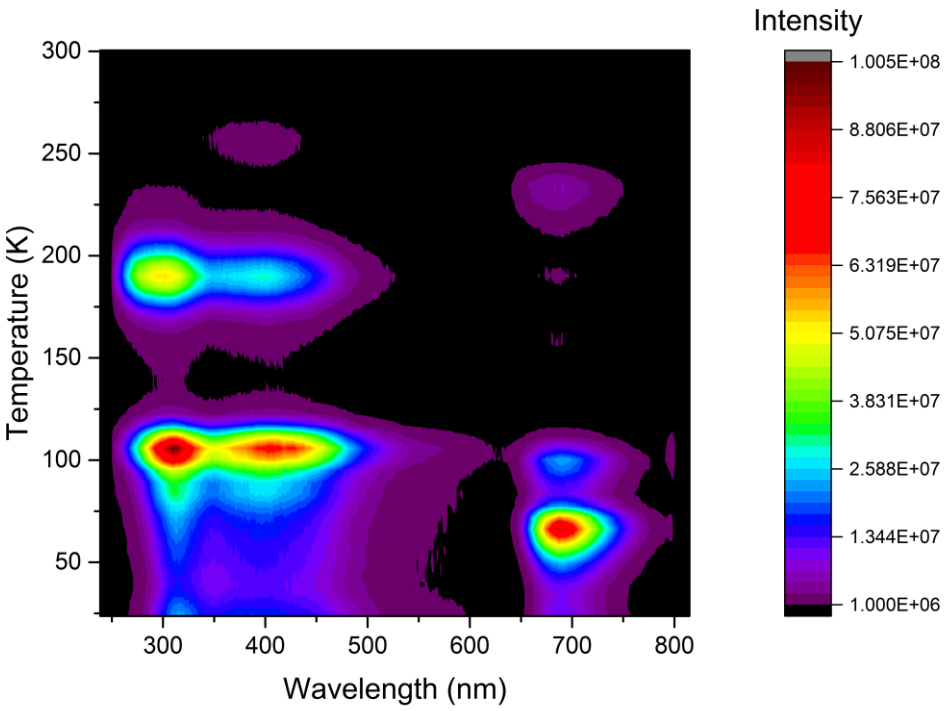

Figure 5: Low Temperature TL of pink sodalite (AF-07-35) as a contour map. Data are system corrected and expressed as arbitrary intensity using the colour scheme on the right. A variety of TL glow peaks are observed at 66, 105, 190 and 232 K, whose responses occur at different wavelengths. The 66 and 232 K TL peaks occur at 690 nm whereas the 105 and 190 K peaks predominantly occur in the UV and blue (309 and 411 nm).

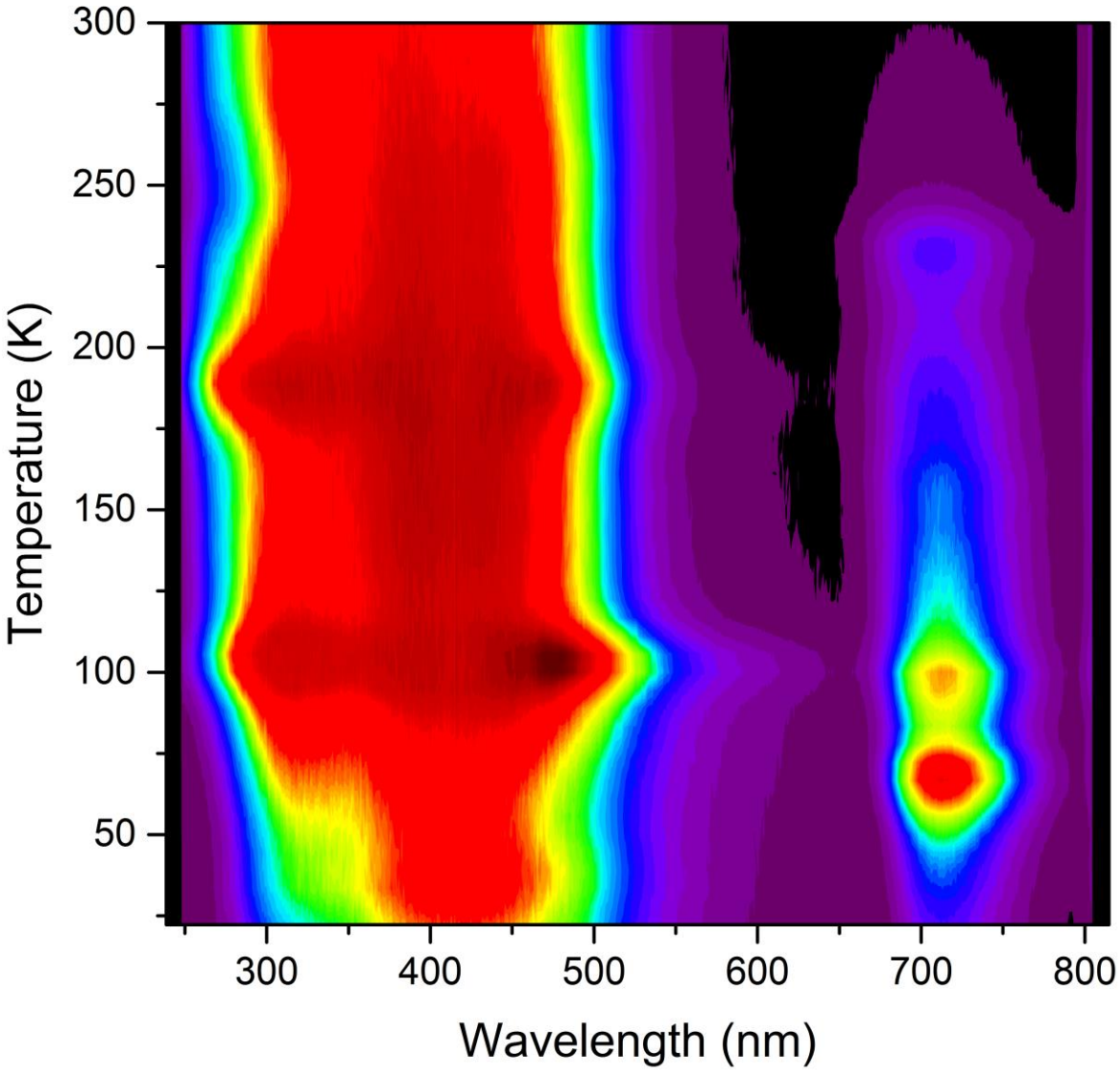

Figure 6: XEOL and TL composite data from pink sodalite (AF-07-35). Where fast ramp rates are employed, XEOL data from the instrument are composites of XEOL and TL. The small peaks in intensity (particularly evident at 690 nm and 66 K) are TL responses (Figure 4) added to the XEOL, better called the XEOLTL response. The true isolated XEOL can be achieved by slowing ramp rates down substantially (although this increases the acquisition times and the data density), or by taking the spectra on the cooling cycle.

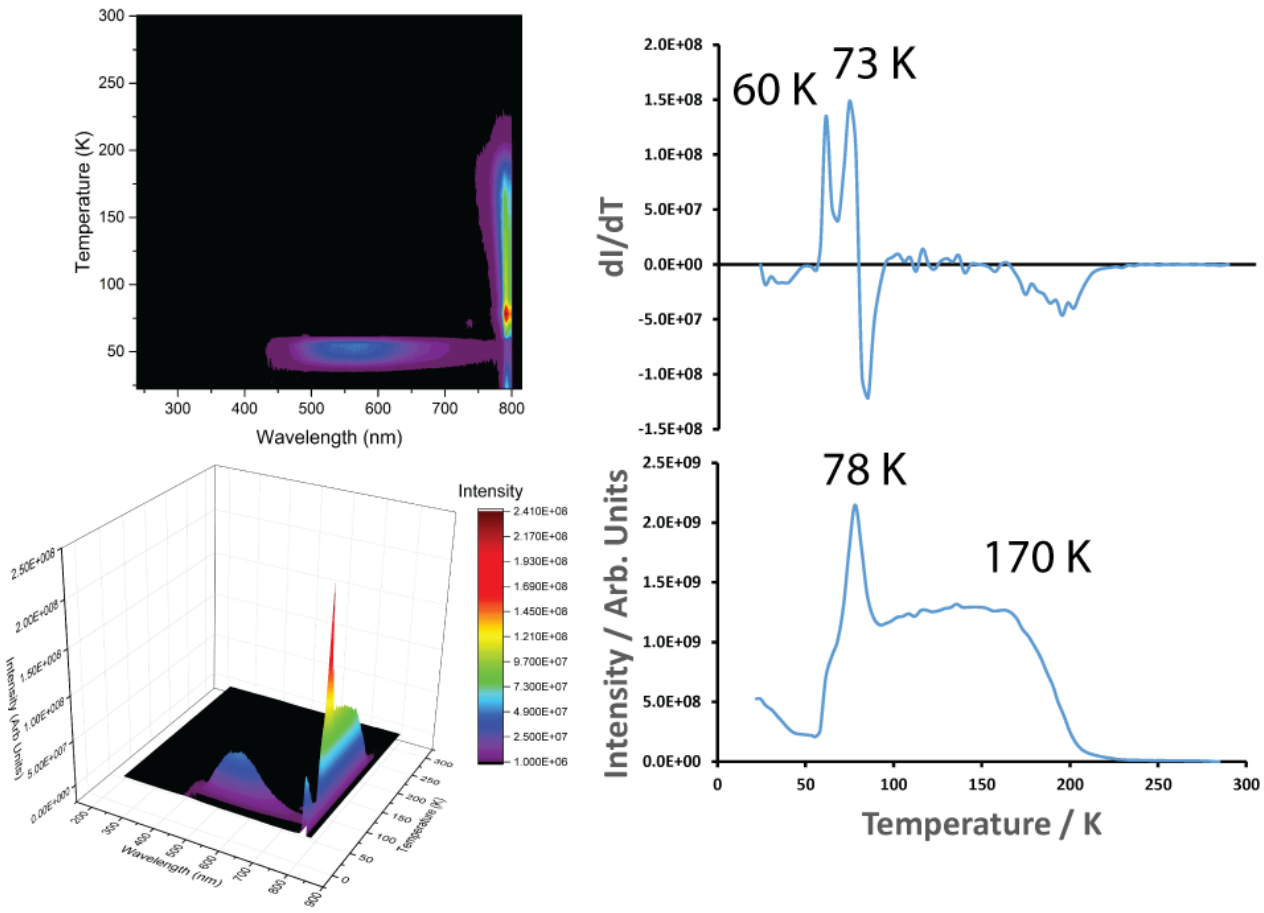

Figure 7: XEOL data from $SrTiO_3$ at 15 kV and 4 mA X-generation. The same data are shown as a 3D graph (top left) and a contour plot (bottom left). The NIR emission at ~794 nm is close to the wavelength limit of the system and the long wavelength part of the emission is truncated. The temperature dependence of the NIR band is shown bottom right. The intense broad band centred at 568 nm has a sharp maximum at 54 K whereas the NIR band at 794 nm has sharp peaks at 24 and 78 K and a minimum at 54 K – precisely the temperature at which the 568 nm band is strongest. The very sudden loss of the orange band on warming to 60 K and the intense NIR band which peaks at 78 K encompass the temperature of a phase transition in $SrTiO_3$ which is expressed very clearly in the data. Phase transitions are often particularly evidence in the first derivative of the data (top right) and we infer the two peaks in the first derivatives define different stages of the phase transition.

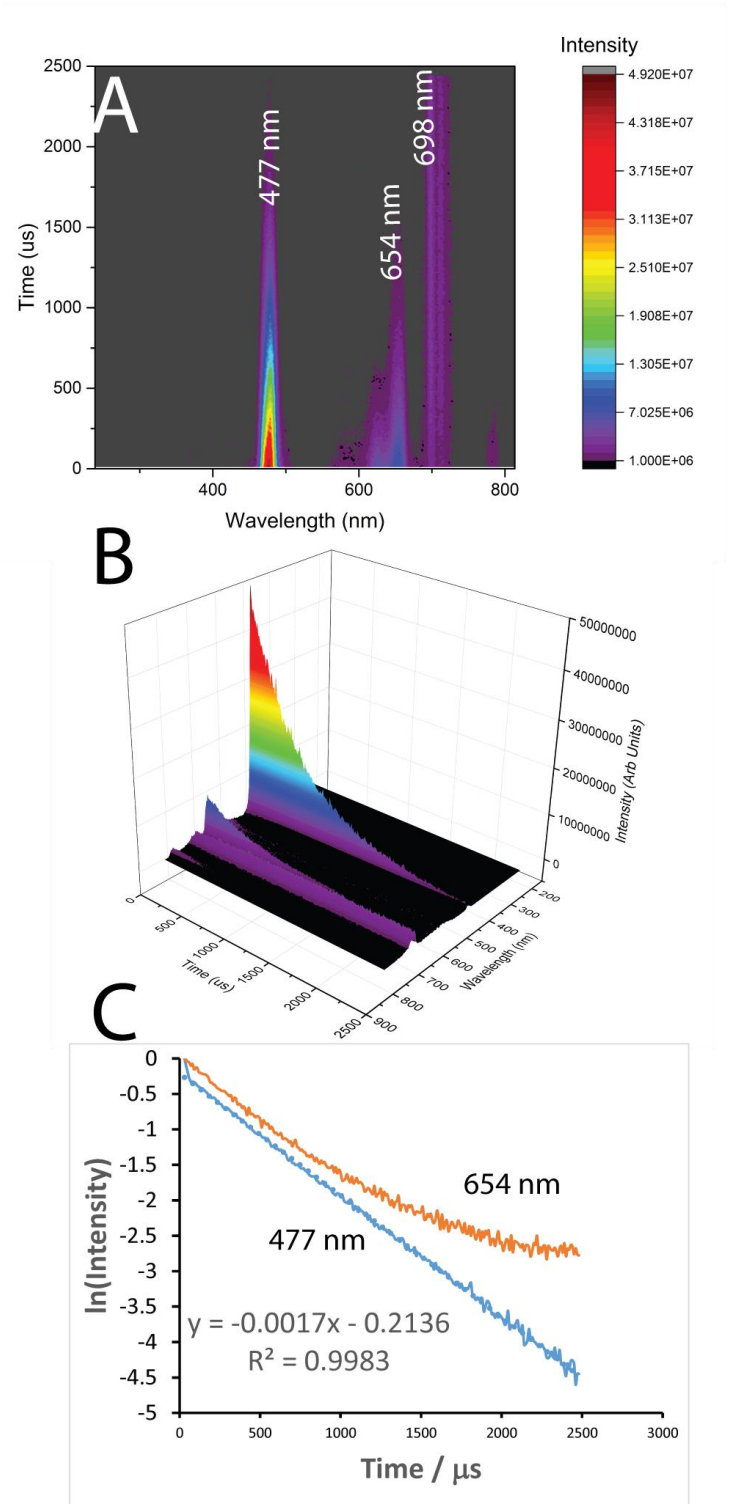

Figure 8: Time-resolved PL of $CaSO_4$:Tm,Li at 155 K. The luminescence intensity as a function of temperature and wavelength is shown in contour (A) and 3D graph formats (C). The decay of the emissions as a function of time is clear for particularly the 477 and 654 nm emissions. A broad emission between 698 and 710 nm is essentially constant over the lifetime of the experiment. The decay profiles of the 477 and 654 nm emissions are fitted in C. The blue component fits a single exponential decay (R^2=0.998) whose slope corresponds to a decay half-life of 582±3 µs; the orange band is initially consistent with this lifetime but the flattening of the data as time increases indicates an additional, longer lifetime component. The intensity of the 697-710 nm region is essentially constant throughout the experiment, showing its half-life is >> 5 ms.